

David A. Johnson

Associate Professor
e-mail: da3johns@uwaterloo.ca

Bryan A. Sperandei

Graduate Student
e-mail: bsperand@uwaterloo.ca

Ross Gilbert

Graduate Student
e-mail: rgilbert@uwaterloo.ca

Department of Mechanical Engineering,
University of Waterloo,
Waterloo, ON N2L 3G1 Canada

Analysis of the Flow Through a Vented Automotive Brake Rotor

Particle image velocimetry (PIV) was used to measure air velocities through a high solidity radial flow fan utilized as an automotive vented brake rotor. A brake rotor is a somewhat unusual fan in that its sole purpose is not to pump air but to dissipate thermal energy, it has no conventional inlet or outlet housing and it has a continuously varying rotational speed. For three typical rotational speeds, the flow characteristics were captured at the inlet and exit of the rotor, as well as internally through the cooling passages. Inlet measurements showed a swirling entry flow condition with significant misalignment of flow onto the vanes. As a result large regions of flow separation were found in the internal vane-to-vane passages on the suction side surfaces, which would lead to poor heat transfer conditions. The main flow exiting the rotor consisted of a series of jets corresponding to the individual rotor passages and were found to be very unstable leading to a rapid decay in velocity. [DOI: 10.1115/1.1624426]

1 Introduction

Automotive brakes are utilized to convert kinetic energy of motion into thermal energy through the friction between stationary brake pads and a rotating surface. Commonly this is done using a cast iron rotating brake rotor with stationary friction surfaces mounted in a caliper. Rotors may be solid disks or two disks separated by a vaned air flow passage (vented rotor). In bringing a vehicle to a stop the brake rotor must be able to store a significant amount of thermal energy since braking occurs in a relatively short period of time. Subsequently, the brake rotor must then dissipate the stored thermal energy quickly in order to be ready for the next application of the brake or friction contact. There are numerous considerations in the design of a vented disk brake rotor and the air flow through the internal passages has previously been of less importance than manufacturing, materials, and structural issues. Improving the rate of heat transfer from a brake rotor will allow for smaller and lighter rotors since the amount of thermal storage required is smaller which will reduce vehicle weight and improve fuel economy. Consequently, vented brake rotors using internal air passages are used in an attempt to increase the level of forced convection and so improve the rate of heat transfer. Early analytical work by Limpert [1] stated that the convective heat transfer coefficient of a vented disk brake rotor is approximately twice that of a solid disk.

Previous work attempting to measure the airflow exiting a brake rotor was completed using pressure based cobra probes, [2–4], to measure the velocity profile in the radial-axial plane at the exit of the rotor but not the radial-angular plane. As well, the inlet and internal passage flow field conditions were not measured. Similar experiments have been carried out on centrifugal fans in water using particle image velocimetry (PIV), [5–8], but the fans tested had volutes, which are never present on an automobile. The purpose of a brake rotor is significantly different due to the thermal energy considerations mentioned above and in that rotors are subject to continuously varying rotational speeds such that the design or operating point can not be defined. Also, the Reynolds numbers examined (ranging from 2.00×10^4 to 1.83×10^5) were lower in those studies than those of the brake rotor in this study (1.82×10^5 to 5.47×10^5). The Reynolds number (Re) is based on the rotor outside diameter and the rotational speed of the rotor,

$$\text{Re} = \frac{\rho \omega D_o^2}{\mu} \quad (1)$$

All measurements were conducted using standard air at 25°C ($\rho = 1.184 \text{ kg/m}^3$, $\mu = 1.85 \times 10^{-5} \text{ kg/ms}$). Three rotor rotational speeds were used for the measurements: 342, 684, and 1026 rpm, representing typical driving speeds of 50, 100, and 150 km/h, respectively. These three speeds resulted in Reynolds numbers of 1.82×10^5 , 3.65×10^5 , and 5.47×10^5 .

The focus of this study was to determine the characteristics of the airflow for a vented brake rotor using PIV (see Adrian [9] and Grant [10] for a detailed description of the PIV technique). Emphasis was placed on determining the air velocity in as many areas in and around the rotor as possible. With PIV, it was possible to locate the internal areas of separation and recirculation, indicating potential areas of poor heat transfer in the rotor. As well, the recording of many images at each location showed the distinction between turbulence-intensive instantaneous vector maps and smooth, low-turbulence averaged velocity values.

2 Experimental Setup

2.1 Apparatus. The design of the experimental test rig required the fulfillment of several criteria to ensure an optimal environment for PIV. A vertical shaft was mounted to a steel test table using two pillow block bearings to ensure smooth rotation of the rotor with minimal runout. The shaft was chain driven via an adjustable speed DC motor. Rotational speed was determined using a tachometer mounted on the motor which was continuously monitored. The end of the shaft was fitted with a production automotive wheel hub in order to mount the brake rotor. The rotor was mounted with the inlet away from the hub in order to keep that region free of any flow obstruction (see Fig. 1). This is an idealized or optimum arrangement in comparison to an automotive wheel assembly where other components obstruct the incoming flow. Figure 2 shows the rotor as installed on a typical automotive front wheel assembly (excluding the rim and tire). In practice flow entering and leaving the rotor will be hindered by the wheel hub, brake caliper, and dust shield, as well as the rim and tire.

The area surrounding the rotor was then enclosed using acrylic panels in order to contain the seeding particles necessary for PIV measurements while maintaining visual access into the test environment. The dimensions of the enclosure ($0.9 \text{ m} \times 0.9 \text{ m} \times 0.61 \text{ m}$) were chosen large enough so as to eliminate any wall effects in the flow field.

Contributed by the Fluids Engineering Division for publication in the JOURNAL OF FLUIDS ENGINEERING. Manuscript received by the Fluids Engineering Division Oct. 1, 2001; revised manuscript received June 4, 2003. Associate Editor: B. Schiavello.

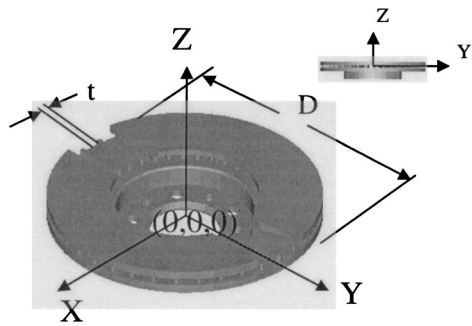


Fig. 1 Vented rotor showing sections removed for internal PIV measurements

2.2 Rotor Geometry. A typical production automotive brake rotor was chosen to represent the radial flow fan used in the PIV experiments. All measurements were performed using this production brake rotor. The cast iron rotor consisted of two flat disks separated by a gap of 8 mm (vane width b) with one disk comprising the hub where the rotor was attached to the rotating shaft. This gap was supported by 37 equally spaced radial vanes. Each disk had an outer diameter (D_o) of 282 mm, and an inner diameter (D_i) of 152 mm. The radial vanes were 54.5 mm in length beginning at a diameter of 168 mm (D_{vi}) and ending at a diameter of 277 mm (D_{vo}) leaving an 8-mm entry distance from the inner radius of the disk to the vane. The purely radial individual vanes were a constant 5.6 mm in thickness (t) from D_{vi} to D_{vo} and were rounded at the entry and exit. This resulted in 37 air flow passages each with a $8.7\text{ mm} \times 8\text{ mm}$ ($w_1 \times b$) entry and a $17.9\text{ mm} \times 8\text{ mm}$ ($w_2 \times b$) exit. For all measurements and results shown in this study, the origin of the cartesian coordinate system was located at the center of rotation of the rotor, and at the mid-width of the air passages between the two disks.

In order to visualize the airflow inside the vent passages, optical access was required in the X - Y plane. This was achieved by removing a section of the upper disk, wide enough to expose at least two full vent passages. The missing section was then replaced with an acrylic window with the same thickness and shape in



Fig. 2 Photograph of a typical front wheel automotive assembly excluding the rim and tire

order to replicate the flow through the passages. An identical window was installed 180 deg from the first in order to balance the rotor and limit vibration (see Fig. 1).

2.3 Particle Image Velocimetry. Simplistically, PIV operates on the basis of capturing images of a fluid flow and determining how far the fluid has moved from one image to the next. In order to visualize an air flow, seed particles are introduced into the flow and are typically illuminated by a high-power pulsed laser light sheet. To illuminate this particular flow, a dual cavity pulsed ($2 \times 120\text{ mJ}$) Nd-YAG laser was used in order to create a light sheet 2–3 mm in thickness spanning the region of interest. Vaporized mineral oil has been shown to follow airflow quite well, [11], and was used as the seeding medium. The smoke was introduced into the enclosure well upstream of the measurement region around the rotor. As well, the smoke was allowed to stabilize in the enclosure before measurements were obtained. To capture images, a CCD camera (Kodak Megaplug ES 1.0) with 1008×1018 pixel resolution was used. The laser and CCD camera were linked through a Dantec Flowmap PIV 1100 processor. Image processing, cross-correlation of the images, and vector validation was performed using an in-house tailored cross-correlation routine.

To determine the displacement of the particles between successive images an iterative multigrid algorithm was used as described by Gilbert [12], which is an advancement of the work of Scarano and Reithmuller [13]. The iterative multigrid technique uses multiple iterations to determine the velocity field with each successive iteration using smaller interrogation areas that have been offset by an integer amount based on the previous iteration's results. The advancement of the technique by Gilbert [12] was to interpolate between vectors when determining the integer offset for each interrogation area, rather than applying the displacement of the nearest velocity vector.

The advantage of the iterative multigrid technique is the ability to use smaller interrogation areas to reduce the magnitude of the velocity gradients within a single interrogation area as well as increasing the resolution of velocity vectors. Smaller interrogation areas could be used with the standard FFT algorithm, [14], but the time separation between the images would have to be reduced, increasing the relative error of the velocity measurement, [12].

The iterative multigrid algorithm used in these experiments applied an iterative approach to the FFT cross-correlation. An initial estimate of the velocity field was determined using the standard FFT cross-correlation scheme. The next iteration then divided the interrogation area into four smaller, equal areas. The new interrogation areas were then displaced by an integer amount based on a bilinear interpolation of the previous velocity estimate and the FFT cross-correlation was performed to refine the velocity estimate. The process was repeated until the interrogation area was reduced to the desired size. Typically, initial interrogation areas of 64×64 pixels were reduced to 16×16 pixels, using 50% overlap in all cases. This resulted in typical interrogation areas ranging of $4.2\text{ mm} \times 4.2\text{ mm}$ (64×64 pixels) down to $1.05\text{ mm} \times 1.05\text{ mm}$ (16×16 pixels) in size. A signal to noise ratio of 1.4 was used in the cross correlation (i.e., any vectors below this signal to noise ratio were discarded). After the final iteration of processing in each experiment, the vector maps contained 15,252 vectors (123×124 vectors).

2.4 Image Orientations. Three distinct flow fields were examined in and around the rotor. In the first setup, the inlet flow entering the air passages along the rotational axis was captured. This was achieved by using a light sheet in the X - Z plane with the region of interest between the center of rotation of the rotor, and inner radius of the upper disk (R_i). The camera was oriented perpendicular to the light sheet and focused on an image area of $85\text{ mm} \times 85\text{ mm}$, resulting in a resolution of 0.084 mm/pixel . The pulses of the laser were left untriggered so as to obtain an average inlet flow at various angular positions of the rotor. The horizontal (X - Y) plane was also measured in order to determine the levels of

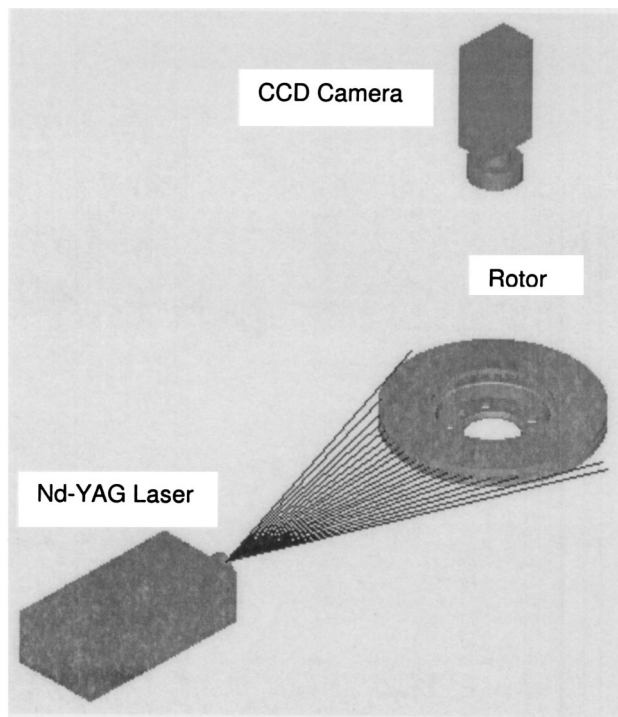


Fig. 3 Orientation of the laser and camera for X-Y plane PIV measurements

swirl present in the flow before entering the rotor. In this case, the camera was suspended above the rotor while the laser formed a horizontal light sheet from one side of the test enclosure (see Fig. 3).

The second test was arranged in order to visualize the internal airflow through the rotor passages. The laser sheet was oriented in the X-Y plane at the midway point ($Z=0$) of the passages (4 mm from either disk). In this case, the laser was triggered to pulse only when an acrylic section of the disk rotated through the camera's field of view. This was done through the use of a stationary optical switch with a single notch on a rotating wheel that interrupted the light beam and ensured that each image captured the same passages. Thus, the use of the word "triggered" will indicate that all images were captured at the same angular position of the rotor every time (phase resolved). Conversely, "untriggered" will indicate images captured at random time intervals, therefore, at no particular position on the rotor. The straight and radial geometry of the vanes allowed the illumination of two full flow passages in each image. The image area in this test was 65 mm \times 65 mm, giving a resolution of 0.064 mm/pixel.

In the third and final test, three different laser and camera configurations were used to capture the airflow exiting the passages at the outer diameter of the rotor. In the first two methods, a light sheet in the X-Y plane was placed just beyond the outer diameter of the rotor, still focused on a 65 mm \times 65 mm area at the middle of the passage width ($Z=0$). The flow was first measured with an untriggered laser pulse for average exit flow conditions, and then repeated with a triggered laser pulse in order to observe the individual jets leaving each flow passage. In the third setup, untriggered images were collected in the X-Z plane so as to view the characteristics of the exiting jets in a vertical plane.

In all cases above, 500 image pairs were collected for each setup and the resultant velocity vectors were ensemble averaged at each position. Each test was repeated for all three rotational speeds. Typical laser pulse separations ranged from 15×10^{-6} to 75×10^{-6} s in order to size the particle displacements appropriately for the interrogation area size.

2.5 Experimental Uncertainty. The rotors used in these studies were actual cast iron production rotors and as a result some geometrical uncertainty existed in the rotor due to its cast manufacturing process. Despite some external machined surfaces, the internal surfaces of the air passages were cast, leaving a comparably rough finish of approximately 0.3 mm. Measurements of the experimental rotor revealed a $\pm 2.3\%$ variation in both the passage height and passage width.

The uncertainty in the machined outer diameter, D_o , of the rotor was determined using manufacturing drawings, while the uncertainty in the rotational speed was determined from tachometer data collected during the measurements. The outer diameter and rotational speeds were found to carry uncertainties of 0.5 mm, and 20 rpm (at all speeds), respectively. This resulted in a Reynolds number uncertainty ranging from 2.3% to 6.2% over the three rotational speeds tested.

For the PIV measurements, the random error due to irregular particles, electronic noise, etc., is shown to be small (<0.07 pixel) by Prasad et al. [15]. For the current measurements, this results in a random error of less than 2% in the determined velocities. The work of Westerweel [16] suggests a typical bias error of 0.05 pixels when using an iterative multigrid algorithm. The resulting bias error in the determined velocities is therefore approximately 1%. Westerweel [17] also suggests a relationship between the particle image diameter and the resulting root-mean-square (RMS) error. Based on the measurements made in this study (average particle image diameters of 2.5 pixels) the expected RMS error is 0.035 pixels, resulting in an additional 0.7% error in the calculated velocities. A detailed analysis of the random, bias, and RMS error associated with PIV is given by Gilbert [12]. Based on the total quoted uncertainty in the calculated velocities (3.7%), the kinetic energy values would have an uncertainty in the range of 5% to 6%.

3 Results and Discussion

3.1 Mean Velocity. Results presented here are all for $Re = 3.65 \times 10^5$ and $N = 684$ rpm as all three rotational speeds gave similar results. For all presented data the axes were made dimensionless by the outer radius of the rotor (i.e., $X^* = X/R_o$, etc.),

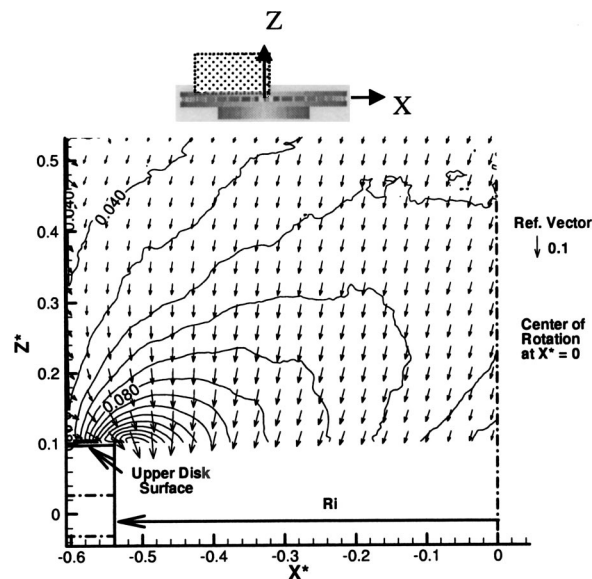


Fig. 4 Absolute mean velocity plot of the inlet flow (X-Z plane at $Y^*=0$), $N=684$ rpm, dimensionless velocity vector=0.1, contours of isovelocity 0.008 dimensionless velocity units, direction of rotation is out of the page

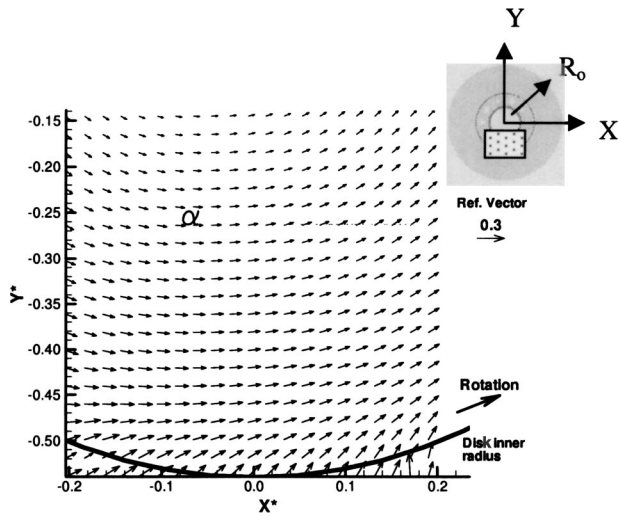


Fig. 5 Absolute mean velocity plot of the inlet flow (X - Y plane at $Z^*=0.1$), $N=684$ rpm, dimensionless velocity vector=0.3

while the mean velocities were normalized by the tangential speed of the rotor at its outer radius, or rotor peripheral speed ($U_o = \omega D_o/2$).

Inlet Flow. Figure 4 shows the mean velocity plot obtained with a vertical light sheet (X - Z plane) at the inlet of the rotor at $Re=3.65 \times 10^5$. The vertical line at $X^*=0$ represents the axis of rotation of the rotor, and the area of visualization extended just beyond the inner radius of the disk (R_i) where the air passage entrances were located. The velocity contour lines in Fig. 4 are separated by increments of 0.008 dimensionless velocity units. Typical radial fan behavior was observed here as the flow was drawn downwards into the center of the rotor before turning 90° in order to enter the air passages. The largest velocity gradient, as shown by the contour lines, occurred near the inner radius of the rotor disk R_i ($X^* \approx -0.54$). Here the flow was drawn in towards the center of the rotor and forced to accelerate around the edge of the disk and into the air passages.

The results obtained in the X - Y plane at $Z^*=0.1$ (1 mm above the upper disk surface) are shown in Fig. 5 and demonstrate the effect of the rotor rotation on the incoming flow.

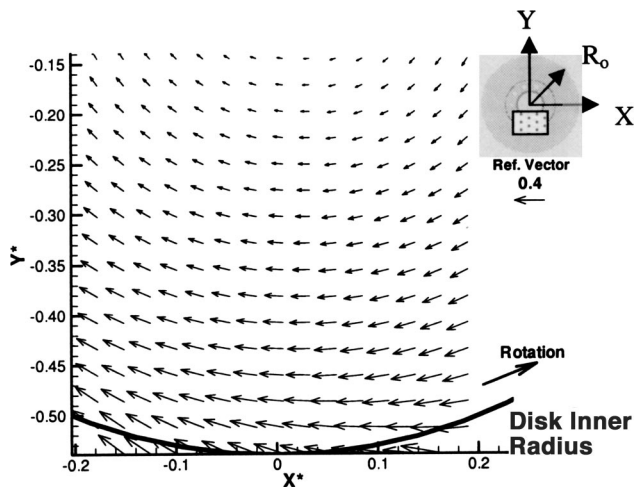


Fig. 6 Relative mean velocity plot of the inlet flow (X - Y plane at $Z^*=0.1$), $N=684$ rpm, dimensionless velocity vector=0.4

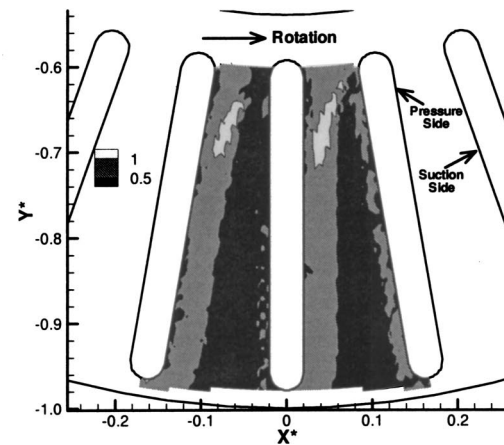
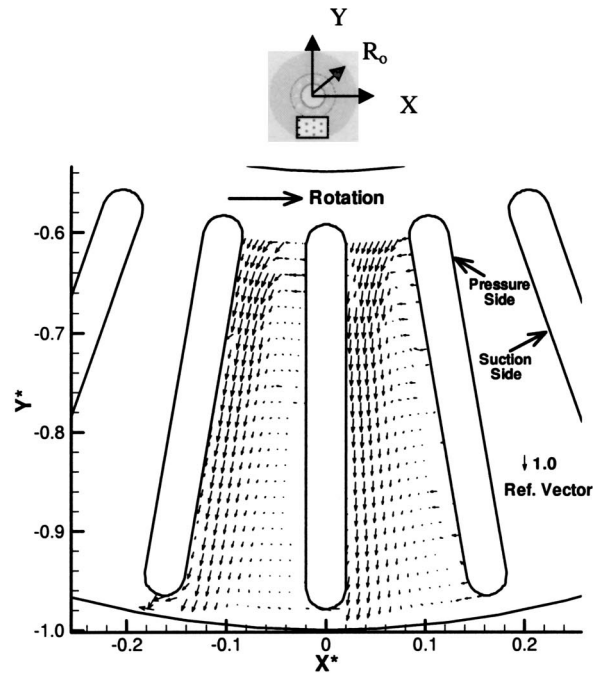


Fig. 7 (a) (Top) relative mean velocity vector plot of the internal flow (X - Y plane at $Z^*=0$), $N=684$ rpm, dimensionless velocity vector=1.0. (b) (Bottom) relative mean velocity contour plot of the internal flow (X - Y plane at $Z^*=0$), $N=684$ rpm.

The shear forces exerted by the counterclockwise rotating upper disk surface imposed a counterclockwise pre-swirl on the inlet flow. In Fig. 6, the local tangential speed (ωr) has been subtracted from the absolute fluid velocities (\mathbf{V}) in Fig. 5 in order to view the velocities relative to the rotor surface (\mathbf{W}). All pre-swirl that does not provide zero incidence onto the vane passages is detrimental. This measured pre-swirl is detrimental as it causes the inlet flow to be further misaligned with the air passages in conjunction with the other vector directions and hence increases shock losses at the vane inlet and reduces or restricts the amount of flow entering the rotor.

Internal Flow (X - Y Plane). The velocity vector plot in Fig. 7(a) and velocity contours in Fig. 7(b) show the relative (\mathbf{W}) mean velocities at the midplane through the air passages. At $Re=3.65 \times 10^5$, the fluid reached maximum internal velocities equal to the rotor peripheral speed (U_o) near the inlet ($-0.64 < Y^* < -0.70$) and along the pressure side decreasing toward the outlet. With counterclockwise rotation, the pressure and suction sides

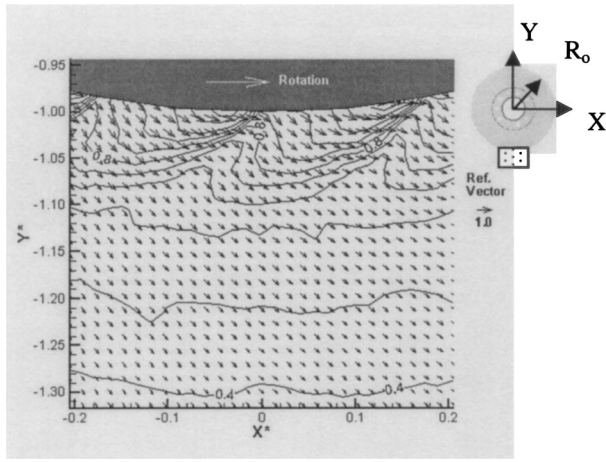


Fig. 8 Absolute mean velocity plot of the exit flow (X - Y plane at $Z^*=0$, triggered), $N=684$ rpm, dimensionless velocity vector =1.0. Contours of isovelocity 0.08 dimensionless velocity units.

were easily identified on the left and right sides of the air passages, respectively. There is significant separation and recirculation on the suction side which will be discussed in a subsequent section. The contour plot shows the correspondence between the measured velocities in the two adjacent passages.

Exit Flow—Horizontal Light Sheet (X - Y Plane). Figures 8 and 9 show the distinction between triggered and untriggered PIV data when measuring the flow exiting the rotor air passages. In both cases, the center of rotation was located at ($X^*=0$, $Y^*=0$) and the rotor vanes imposed both a radial and tangential velocity component on the exiting flow. Both figures show the average of 500 image pairs. The images used for Fig. 8 were all taken at the same rotational position as that in Figs. 7(a), 7(b) (one vane aligned vertically with the line $X^*=0$). In contrast, the 500 images used for Fig. 9 were taken at random rotational positions. In the triggered case (Fig. 8), the contour lines show the effects of the individual rotor vanes, as the exit velocities fluctuate in magnitude and direction depending on their location within the region $-1.05 < Y^* < -1.00$ (velocity contour lines in both Figs. 8 and 9 are separated by increments of 0.08). These effects were removed by averaging with the untriggered measurements, as the contour

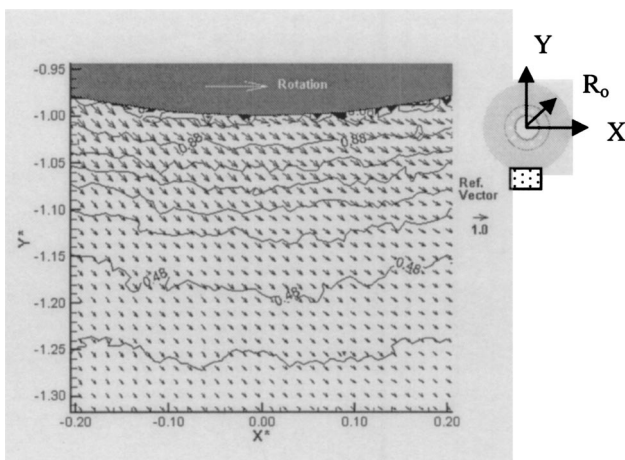


Fig. 9 Absolute mean velocity plot of the exit flow (X - Y plane at $Z^*=0$, untriggered), $N=684$ rpm, dimensionless velocity vector =1.0. Contours of isovelocity 0.08 dimensionless velocity units.

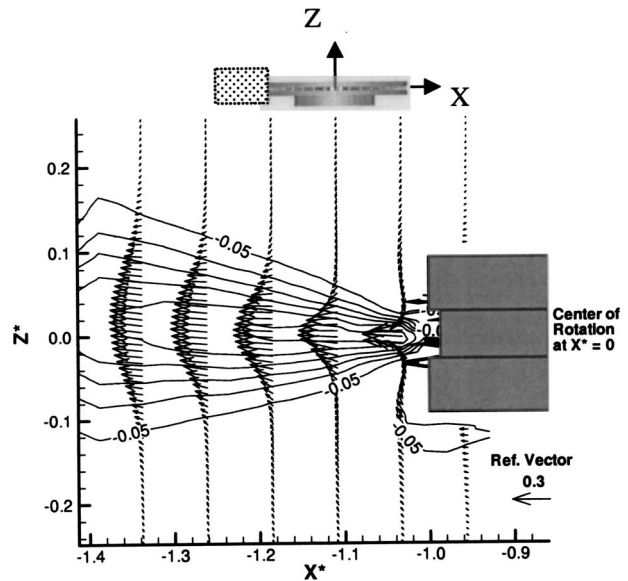


Fig. 10 Absolute mean velocity plot of the exit flow (X - Z plane at $Y^*=0$), $N=684$ rpm, dimensionless velocity vector =0.3. Contours of isovelocity 0.05 dimensionless velocity units.

lines of Fig. 9 show little variation in velocity along lines of constant radius. The triggered measurements effectively showed a phase averaged picture of the flow at one rotor location, with peak fluid absolute velocities exceeding $1.1 \cdot U_o$. When untriggered, an average of many random instantaneous pictures was observed, and the peak velocities measured were therefore lower at $0.95 \cdot U_o$, but were more representative of the overall flow rate achieved through the rotor.

Exit Flow—Vertical Light Sheet (X - Z Plane). The use of a vertically oriented light sheet revealed the behavior of the exit flow as a free jet. Figure 10 shows a side view (X - Z plane) of the rotor at D_o with several exit velocity profiles plotted downstream. Note that the velocity profiles in Fig. 10 represent only the radial component (V_x) of the absolute exit velocity. The velocity contour lines in Fig. 10 are separated by increments of 0.05 dimensionless velocity units. Similar to typical free jet behavior, the profiles steadily decayed with increasing downstream distance (increasing negative X^*). Near the rotor, the profile was narrow and peaked at $0.4 \cdot U_o$, while further downstream at $X^* = -1.32$ the profile was much wider and decayed to a peak velocity of $0.25 U_o$. It is important to note that the velocity profiles in Fig. 10 represent only the radial component (V_x) of the absolute exit velocity, when, in fact, the jets also contain a significant tangential component (V_y), as shown in the X - Y plane (Fig. 9). The direction of the velocity vectors outside of the jet core in Fig. 10 indicated a significant amount of entrainment by the jet. This averaged picture is in contrast to Fig. 11 which shows one of the 500 instantaneous vectors maps used to ensemble average Figure 10. Here, the turbulence and instability in the free jet was apparent. Downstream vortical structures are dimensionally similar to the rotor exit passage dimension.

3.2 Kinetic Energy

Inlet Flow. The turbulent kinetic energy, K_t , was defined using the fluctuating velocity components, u' and v' .

$$K_t = \frac{u'^2 + v'^2}{2} \quad (2)$$

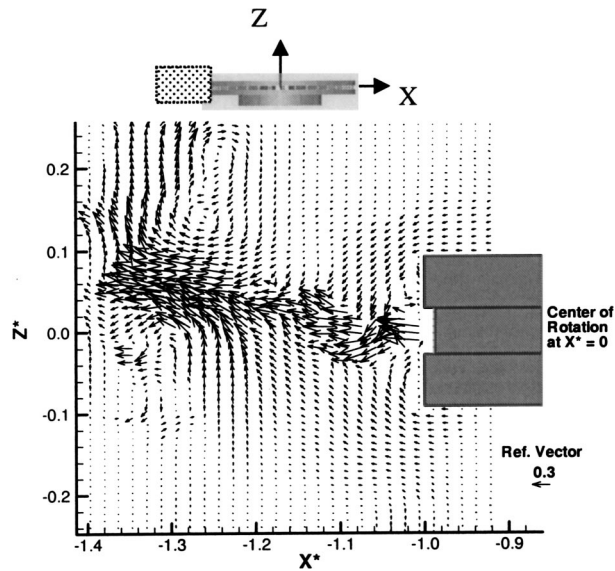


Fig. 11 Absolute mean velocity plot of the exit flow (X - Z plane at $Y^*=0$, single instantaneous vector map), $N=684$ rpm, dimensionless velocity vector=0.3

The values of K_t were then nondimensionalized by U_o^2 , the square of the rotor peripheral velocity. Levels of K_t^* were found to fluctuate in a manner similar to the mean velocity plots, with the highest levels occurring in the areas of highest mean velocity gradients. The highest measured values of turbulent kinetic energy occurred at the inlet near the inner diameter of the disk, D_i , where the flow was forced to accelerate around the disk in order to enter the air passages ($X^* \approx -0.55$, $Z^* \approx 0.1$ from Fig. 4). In this area, K_t^* values of 0.0056 were observed, compared to an average of 0.0025 throughout the rest of the plotted area in Fig. 4.

Internal Flow. The flow through the air passages displayed the highest turbulent kinetic energy levels in the middle of the passage, along the geometric division line between the pressure and suction side. Here, K_t^* levels peaked at 0.06 and were observed to decrease gradually throughout the passage length to 0.01 at the exit (see Fig. 12).

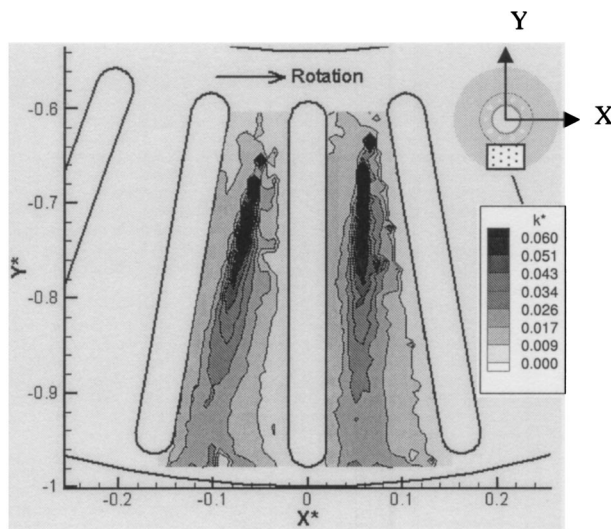


Fig. 12 Nondimensionalized turbulent kinetic energy plot of the internal flow (X - Y plane at $Z^*=0$), $N=684$ rpm

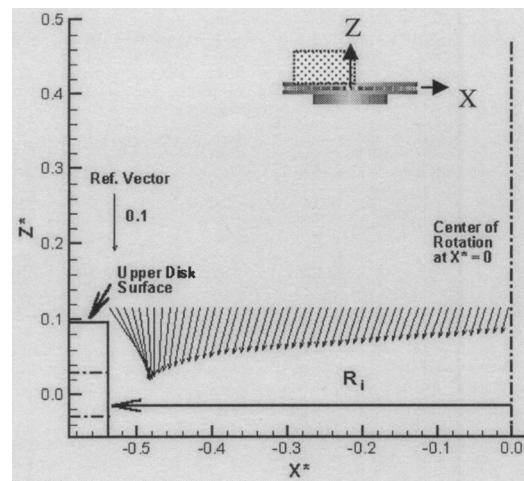


Fig. 13 Inlet velocity profile used to calculate the mass flow entering the rotor, $N=684$ rpm. Rotation out of the page. Dimensionless velocity vector=0.1.

Exit Flow. External to the rotor, the highest levels of turbulent kinetic energy occurred periodically behind each passing vane. For example, the vane oriented with the $X^*=0$ axis in Fig. 8 induced the highest turbulence levels at $X^* \approx -0.045$ and $Y^* \approx -1.03$, an area which trails the tip of the vane as it passes. This area had a turbulent kinetic energy level of 0.046 compared to 0.020 in surrounding areas.

Of all the measured flow areas, turbulent kinetic energy values were highest in the internal passages.

3.3 Flow Balance

Inflow. One method of comparing the experimental results was to compare the volumetric flow rates into and out of the rotor based on the velocity profiles obtained from the PIV measurements. In order to determine the inflow, a representative inlet velocity profile (V_z) was chosen along the upper disk surface ($Z^* \approx 0.1$) plane between the center of rotation ($X^*=0$) and the edge of the inner radius ($X^*=0.54$) as close to the upper disk surface

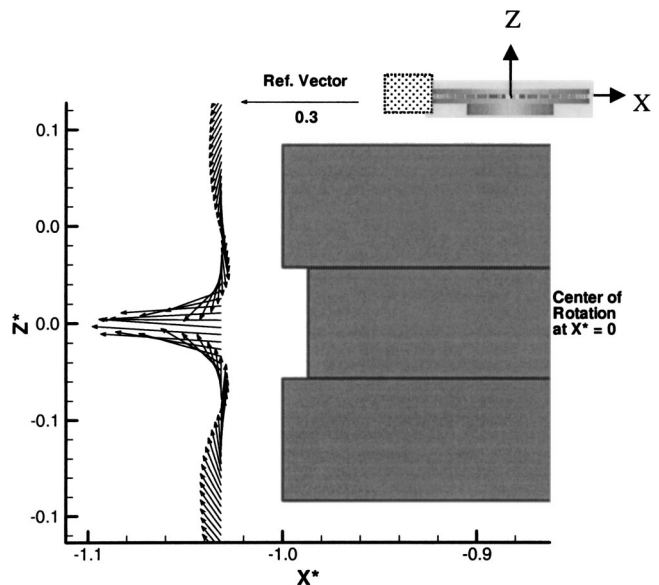


Fig. 14 Exit velocity profile used to calculate the mass flow exiting the rotor, $N=684$ rpm. Dimensionless velocity vector=0.3.

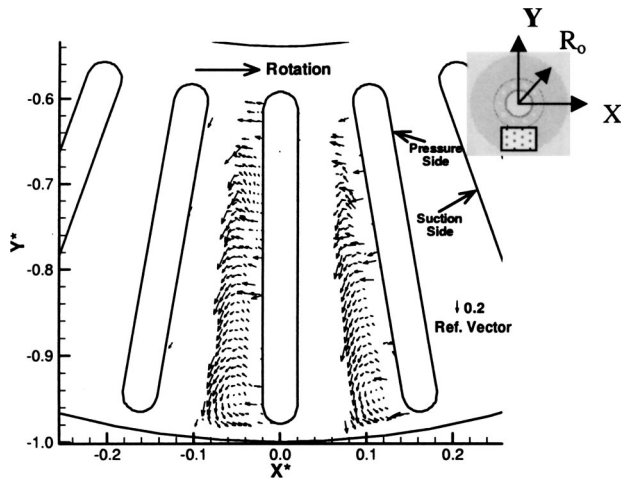


Fig. 15 High resolution vector plot of internal flow (pressure side vectors removed for clarity), $N=684$ rpm. Dimensionless velocity vector=0.2.

as possible. This velocity profile was then revolved 360 deg in order to encompass the entire possible inlet area of the rotor (Fig. 13). The volumetric inflow as represented by the flow number

$$\phi = \frac{Q}{\omega D_o^3}, \quad (2)$$

was thus calculated from the PIV results to be $\phi_{PIV,i}=0.0115$.

Outflow. The velocity profile used in the calculation of the exit flow is shown in Fig. 14. The radial velocities (V_x) in the profile were integrated between $Z^* = \pm 0.028$ and revolved around the outer diameter of the rotor to yield $\phi_{PIV,o}=0.0105$ nondimensional flow units (also determined from the PIV results). This value is comparable to the calculated inflow, although it is lower, leaving a difference of 8.2%. This difference is reasonable given the assumptions made and the integration method utilized to determine the flow rate and it may indicate some mass flow bypassing the inlet and flowing over the upper disk surface due to the position of the inlet flow control volume.

3.4 Separation Points. There are significant regions of flow separation in the internal flow passages of the rotor as shown in the relative velocity vector plots (Figs. 7(a) and 7(b)). These plots show large areas of little or no flow in the X - Y plane along the entire right (suction) side of the passage. Flow separation began

immediately after the passage entrance. The dominant cause of this is the misalignment between the physical radially outward vane angle (90 deg to the tangential direction in the X - Y plane) and the relative velocity approaching the vane as seen in Fig. 6 (dominant tangential velocity direction) and Fig. 4 (minor axial velocity direction). Thus the inlet relative velocity is perpendicular to the physical vane and the incidence angle is very large. Figure 15 re-plots Fig. 7(a) with increased vector lengths on the suction side of the passage. Out of plane effects not measured by the planar PIV system are likely significant in this region due to the reverse flow measured near the vane, close to the leading edge (entrance) as well as a recirculation zone centered near the vane trailing edge.

The flow through the radial vanes of the rotor may also be treated as a flow through a rotating diffuser. The study by Rothe and Johnston [18] provide relationships between the Reynolds number Re_Q , rotation number, Ro , and the area ratio between the outlet and inlet area of a diffuser. Re_Q is the Reynolds number based on the inlet flow area,

$$Re_Q = \frac{w_1(Q/A)}{\nu} \quad (3)$$

while Ro is defined as,

$$Ro = \frac{\omega \cdot w_1}{(Q/A)} \quad (4)$$

The area ratio, AR , is defined as the flow area at the trailing edge (R_{vo}) over the flow area at the leading edge of the rotor (R_{vi}), and was constant for all vanes at 2.06, and at a Re of 3.65×10^5 , Re_Q , was 3300 and the rotation number, Ro , was 0.11. Based on these characteristics, this flow falls within a region of two-dimensional stall in [18]. This is due in part to the included expansion angle (9.65 deg) of each air passage which in itself is not enough to cause the level of separation measured. As well, Rothe and Johnston [18] suggest that the presence of rotation increases the tendency for stall in the air passage by suppressing the turbulent mixing and shear stress of the Coriolis acceleration field.

3.5 Independence of Rotational Speed. Figure 16 plots the maximum resultant exit velocities (V_{res}) of the airflow at the three rotational speeds tested. When the velocities were normalized by the peripheral velocity (U_o) of the rotor, a near constant value of 0.895 was observed, indicating a linear relationship between the rotational speed and the volume of airflow in the rotor over the range of speeds tested.

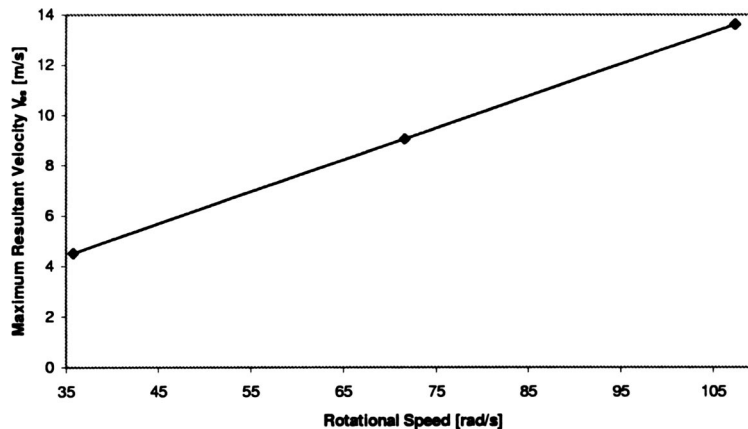


Fig. 16 Relationship between the maximum exit flow velocities and the rotational speed of the rotor

4 Conclusions

PIV measurements of a rotating automotive brake rotor revealed interesting information about the flow structure through the radial vaned air passages. The presence of large separation areas in the air passages indicated poor performance as a radial flow fan. This is caused by the high incidence angle due to misalignment between the relative velocity direction and the physical blade angle. An additional factor was the effect of rotation, where rotation number and diffuser area ratio were used to predict stall. The areas of highest turbulent kinetic energy were found to occur through the middle of the air passages, where large velocity gradients separated the pressure and suction sides. Normalized mean velocity plots showed little variation at the three rotational speeds tested, indicating a linear relationship between the velocities established in the rotor and rotational speed.

These results will serve as useful information towards improving the geometry of the air passages in automotive brake rotors. Improved geometry will result in improved flow through each air passage, making the rotor more efficient in moving air. Further tests are recommended in this aspect in order to verify a relationship between improving the air flow and improving the heat dissipation of the rotor. These rotors operate over a very wide range of rotational speeds and a 'best design' for one flow would not characteristically apply to all flow ranges. It is important to note however, that all rotors were tested without any obstructions at the inlet or outlet, and hence, the best possible performance was measured. The inlet and the entire rotor can become severely blocked by other components such as drive shafts and wheel hubs in full automotive wheel assemblies.

Acknowledgments

The authors would like to acknowledge the financial support of the Natural Sciences and Engineering Research Council of Canada (NSERC).

Nomenclature

A	= cross-sectional area of rotor air passage inlet (mm^2) ($A = w_1^* b$)
AR	= area ratio (w_2/w_1)
b	= space between the two brake disks
D_o, D_i	= disk outer and inner diameter, respectively (mm)
D_{vo}, D_{vi}	= vane outer and inner diameter, respectively (mm)
Q	= flow rate (volumetric) (m^3/s)
R_o, R_i	= disk outer and inner radius, respectively (mm)
R_{vo}, R_{vi}	= vane outer and inner radius, respectively (mm)
Re	= rotational Reynolds number
Re_q	= Reynolds number based on inlet channel height
RO	= rotation number
V_{res}	= absolute resultant air velocity (radial and tangential component) $V_{res} = \sqrt{V_x^2 + V_y^2}$
w_1, w_2	= distance between rotor vanes inlet, outlet, respectively (mm)
X^*	= represents radial or tangential direction as indicated in each figure ($X^* = X/R_o$)

Y^* = represents radial or tangential direction as indicated in each figure ($Y^* = Y/R_o$)

Z^* = axial direction ($Z^* = Z/R_o$)

Subscripts

i, o = inlet and outlet, respectively

Greek Symbols

μ = absolute viscosity (kg/ms)

ν = kinematic viscosity (m^2/s)

θ = angular direction

ρ = density (kg/m^3)

ϕ = overall flow number ($Q/\omega D_o^3$)

$\phi_{PIV,i}$ = overall inlet flow number based on PIV results

$\phi_{PIV,o}$ = overall outlet flow number based on PIV results

ω = rotational speed (1/s)

References

- [1] Limpert, R., 1975, "Cooling Analysis of Disc Brake Rotors," SAE Paper No. 751014.
- [2] Sisson, A. E., 1978, "Thermal Analysis of Vented Brake Rotors," SAE Paper No. 780352.
- [3] Hudson, M. D., and Ruhl, R. L., 1997, "Ventilated Brake Rotor Air Flow Investigation," SAE Paper No. 971033.
- [4] Jerhamre, A., and Bergstrom, C., 2001, "Numerical Study of Brake Disc Cooling Accounting for Both Aerodynamic Drag Force and Cooling Efficiency," SAE Paper No. 2001-01-0948.
- [5] Paone, N., Riethmuller, M. L., and Van den Braembussche, R. A., 1989, "Experimental Investigation of the Flow in a Vaneless Diffuser of a Centrifugal Pump by Particle Image Displacement Velocimetry," *Exp. Fluids*, **7**, pp. 371–378.
- [6] Shepherd, I. C., and La Fontaine, R. F., 1993, "Mapping the Velocity Field in a Centrifugal Fan Using Particle Image Velocimetry," *J. Wind. Eng. Ind. Aerodyn.*, **50**, pp. 373–382.
- [7] Shepherd, I. C., La Fontaine, R. F., Welch, L. W., and Downie, R. J., 1994, "Velocity Measurement in Fan Rotors Using Particle Image Velocimetry," *Laser Anemometry*, ASME, New York, FED-Vol. 191, pp. 179–183.
- [8] Akin, O., and Rockwell, D., 1994, "Flow Structure in a Radial Flow Pumping System Using High Image Density Particle Image Velocimetry," *ASME J. Fluids Eng.*, **116**, pp. 538–544.
- [9] Adrian, R. J., 1991, "Particle-Imaging Techniques for Experimental Fluid Mechanics," *Annu. Rev. Fluid Mech.*, **23**, pp. 261–304.
- [10] Grant, I., 1997, "Particle Image Velocimetry: A Review," *Proc. Inst. Mech. Eng., Part C: J. Mech. Eng. Sci.*, **211**, pp. 55–76.
- [11] Melling, A., 1997, "Tracer Particles and Seeding for Particle Image Velocimetry," *Meas. Sci. Technol.*, **8**, pp. 1406–1416.
- [12] Gilbert, R., 2001, "Evaluation of FFT Based Cross-Correlation Techniques Used in Particle Image Velocimetry," M.A.Sc. thesis, University of Waterloo, Waterloo, Canada.
- [13] Scarano, F., and Riethmuller, M. L., 1999, "Iterative Multigrid Approach in PIV Image Processing With Discrete Window Offset," *Exp. Fluids*, **26**, pp. 512–523.
- [14] Willert, C. E., and Gharib, M., 1991, "Digital Particle Image Velocimetry," *Exp. Fluids*, **10**, pp. 181–193.
- [15] Prasad, A. K., Adrian, R. J., Landreth, C. C., and Offutt, P. W., 1992, "Effect of Resolution on the Speed and Accuracy of Particle Image Velocimetry Interrogation," *Exp. Fluids*, **13**, pp. 105–116.
- [16] Westerweel, J., 1997, "Fundamentals of Digital Particle Image Velocimetry," *Meas. Sci. Technol.*, **8**, pp. 1379–1392.
- [17] Westerweel, J., 2000, "Theoretical Analysis of the Measurement Precision in Particle Image Velocimetry," *Exp. Fluids*, (Suppl.), pp. S3–S12.
- [18] Rothe, P. H., and Johnston, J. P., 1976, "Effects of System Rotation on the Performance of Two-Dimensional Diffusers," *ASME J. Fluids Eng.*, **9**, pp. 422–430.